The Astrophysical Journal, 901:64 (9pp), 2020 September 20 https://doi.org/10.3847/1538-4357/abada6

Active Region Irradiance during Quiescent Periods: New Insights from Sun-as-a-star Spectra

Maria D. Kazachenko[1,2] and Hugh S. Hudson[3,4]
[1] Department of Astrophysical and Planetary Sciences, University of Colorado Boulder, 2000 Colorado Ave, Boulder, CO 80305, USA
maria.kazachenko@colorado.edu
[2] National Solar Observatory, University of Colorado Boulder, 3665 Discovery Drive, Boulder, CO 80303, USA
[3] Space Sciences Laboratory, University of California–Berkeley, Berkeley, CA 94720, USA
[4] SUPA School of Physics & Astronomy, University of Glasgow, UK
Received 2020 July 1; revised 2020 July 27; accepted 2020 August 7; published 2020 September 22

Abstract

How much energy do solar active regions (ARs) typically radiate during quiescent periods? This is a fundamental question for storage and release models of flares and ARs, yet it is presently poorly answered by observations. Here we use the "Sun-as-a-point-source" spectra from the EUV Variability Experiment (EVE) on the Solar Dynamics Observatory to provide a novel estimate of radiative energy losses of an evolving AR. Although EVE provides excellent spectral (5–105 nm) and temperature (2–25 MK) coverage for AR analysis, to our knowledge, these data have not been used for this purpose due to the lack of spatial resolution and the likelihood of source confusion. Here we present a way around this problem. We analyze EVE data time series, when only one large AR 11520 was present on the disk. By subtracting the quiet-Sun background, we estimate the radiative contribution in EUV from the AR alone. We estimate the mean AR irradiance and cumulative AR radiative energy losses in the 1–300 Å and astronomical standard ROSAT-PSPC, 3–124 Å, passbands and compare these to the magnetic energy injection rate through the photosphere, and to variations of the solar cycle luminosity. We find that while AR radiative energy losses are ∼100 times smaller than typical magnetic energy injection rates at the photosphere, they are an order of magnitude larger or similar to the bolometric radiated energies associated with large flares. This study is the first detailed analysis of AR thermal properties using EVE Sun-as-a-star observations, opening doors to AR studies on other stars.

Unified Astronomy Thesaurus concepts: Solar active regions (1974); Active solar corona (1988); Solar spectral irradiance (1501); Solar activity (1475); Solar physics (1476); Solar coronal lines (2038); Solar active region magnetic fields (1975); Stellar activity (1580); Solar atmosphere (1477); Solar flares (1496); Solar flare spectra (1982); Stellar spectral lines (1630)

1. Introduction

The evolution of an active region (AR) in the solar corona reflects the evolution of the photospheric magnetic fields connected to it (see the review by van Driel-Gesztelyi & Green 2015). Many multiwavelength analyses have studied the long-term evolution of ARs, including the behavior of the magnetic field and its nonpotentiality (e.g., Démoulin et al. 2002), flare and CME activity (e.g., Iglesias et al. 2019), helicity budget (e.g., Liu & Schuck 2012), coronal heating (e.g., Warren et al. 2012; Reva et al. 2018), coronal intensity, temperature and emission measure (e.g., Fisher et al. 1998; Tripathi et al. 2011; Ugarte-Urra et al. 2017), and total irradiance (e.g., Ortiz et al. 2004; Zahid et al. 2004).

While many aspects of long-term AR evolution have been well studied (van Driel-Gesztelyi & Green 2015), we are still missing quantitative observational estimates of how much energy ARs lose to radiation as they evolve. Specifically, how much of the magnetic energy injected as Poynting flux through the photosphere is lost due to radiation? This estimate is essential to constrain the total energy budget of the AR. In principle, the Poynting flux should match the budget of magnetic energy stored in the AR and its radiative (and other) energy losses. In practice, however, most of the current approaches estimate AR total magnetic energy as a cumulative sum of the photospheric Poynting fluxes (Liu & Schuck 2012; Tziotziou et al. 2013; Kazachenko et al. 2015; Vemareddy 2015; Lumme et al. 2019), neglecting radiative energy losses.

Deriving radiative energy losses from the observations requires broad spectral measurements covering a range of characteristic temperatures. Here the EUV Variability Experiment (EVE; Woods et al. 2012) on board the Solar Dynamics Observatory (SDO; Pesnell et al. 2012) has ideal properties spectroscopically. It acquires continuous full-disk EUV spectra of Sun-as-a-star in the range of 5–105 nm every 10 s with a spectral resolution of 0.1 nm and an excellent signal-to-noise ratio. The MEGS-A component of EVE in particular contains a wide variety of iron emission lines formed around $10^{5.7}$–$10^{6.8}$ K (0.5–6.3 MK), making it an excellent basis for studying solar temperature profiles during both active and quiescent periods.

Although EVE provides full spectral coverage for AR analysis, to our knowledge, no EVE data have been used explicitly for AR analysis. The main reason for this is lack of spatial resolution in EVE observations—since EVE observes the Sun-as-a-star spectrum, it cannot simply distinguish between AR and quiet-Sun contributions. However, when only one AR is present on the disk we can subtract the Sun-as-a-star spectrum when no ARs are present (the quiet-Sun spectrum), to derive the spectrum of the AR alone. In this paper, we use such EVE difference spectra to first find the differential emission measure (DEM) of the AR and then use it to quantify AR radiative energy losses as a function of time in the 1–300 Å spectral range.

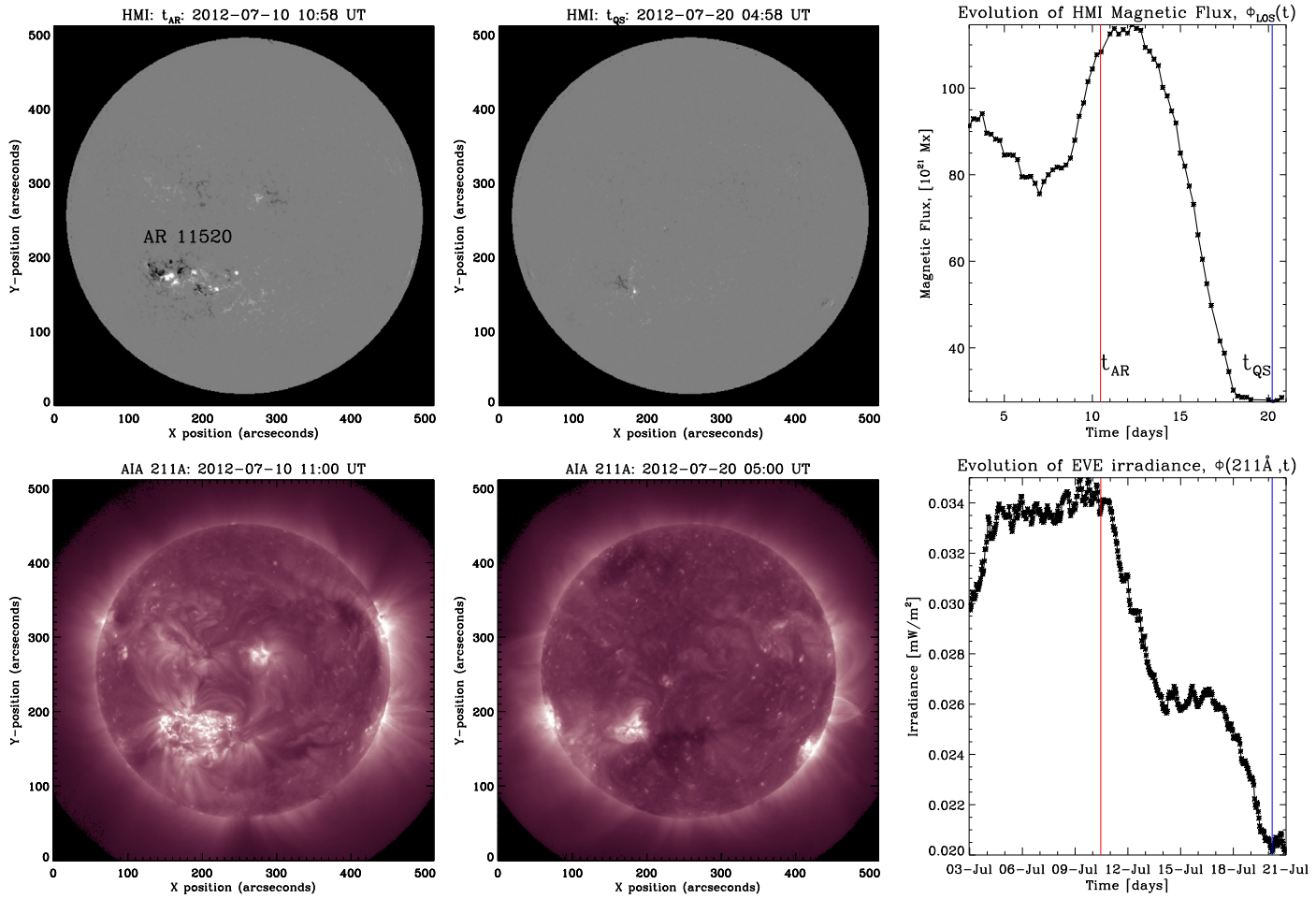

Figure 1. AR 11520: HMI LOS magnetic field (top) and AIA 211 Å maps (bottom) around AR and quiet-Sun times, t_{AR} = July 10 10:59 UT (left) and t_{QS} = July 20 04:59 UT (middle), respectively. The right column shows the evolution of HMI disk-integrated unsigned LOS magnetic flux, $\Phi_{LOS}(t)$, and Fe XIV 211 Å EVE irradiance (line-integrated spectrum), Φ(211Å, t), as AR 11520 crossed the disk. The vertical red and blue dotted lines show t_{AR} and t_{QS}, respectively. See Section 2.

The Sun-as-a-star approach here explicitly relates to the solar irradiance at 1 au, equivalent to an astronomical "spectral energy distribution". The standard solar reference work for AR luminosity remains the classical review of Withbroe & Noyes (1977), which focused on assessing the luminosity as a surface brightness, as related to classical 1D semi-empirical model atmospheres. Our approach here results in the estimates of the luminosity, L_{AR}, of an AR during its disk passage, which we compare with the total unsigned magnetic flux of the region (see Fisher et al. 1998) and the magnetic energy flux through the photosphere, the Poynting flux.

The paper is organized as follows. In Section 2, we describe the EVE data during a passage of AR 11520 and the analysis we used to find fluxes in lines of interest. In Section 3, we describe the methods we use to find AR DEMs and AR radiative losses. In Section 4 we present DEMs from EVE and compare them with DEMs derived from the averaged intensities from the Atmospheric Imaging Assembly (AIA; Lemen et al. 2012) data; we show how the region's DEM evolves as a function of time, derive its radiative losses and total radiated energy, and compare our results with previous scaling relationship between AR X-ray emission and magnetic flux (Fisher et al. 1998). Finally, in Section 5, we summarize our results and draw conclusions, including comparisons with the classical reference of Withbroe & Noyes (1977).

2. Data: EVE Observations of AR 11520

We selected AR 11520 for this study, as shown in Figure 1. This region was the only AR present on the solar disk from its central meridian crossing (~2012 July 11) to its disappearance over the east limb, allowing us to attribute the disk-integrated properties to this region over this interval. Specifically, AR 11520 appeared on the east limb on t_{East} = 2012 July 5 (S15E70), crossed the central meridian on t_{CM} = 2012 July 12 (S16W08) and disappeared behind the west limb on t_{West} = 2012 July 18 (S17W89). The Sun did not have any large ARs on 2012 July 20, hence we chose t_{QS} = 2012 Jul 20 05:00 UT as the quiet-Sun reference time. We chose t_{AR} = 2012 July 10 11:00 UT as the primary sample time, when the AR was 15° east from the central meridian; t_{AR} corresponded to a quiescent period of AR evolution 1 hr after a C2.0-class flare. As AR 11520 crossed the disk, it hosted one X1.4 flare on 12 July 2012, four M-class flares (M1.1, M2.0, M1.7, M1.0), and 37 C-class flares.

Figure 1 illustrates the temporal evolution of image-resolved magnetic field and EUV 211 Å irradiance: the left and middle columns show line-of-sight (LOS) magnetic field maps from the Helioseismic and Magnetic Imager (HMI; Schou et al. 2012) and 211 Å images from AIA at t_{AR} and t_{QS}, respectively. The right column shows the evolution of disk-integrated LOS magnetic flux, $\Phi_{LOS}(t)$, and the 211 Å irradiance, Φ(211Å, t), over the

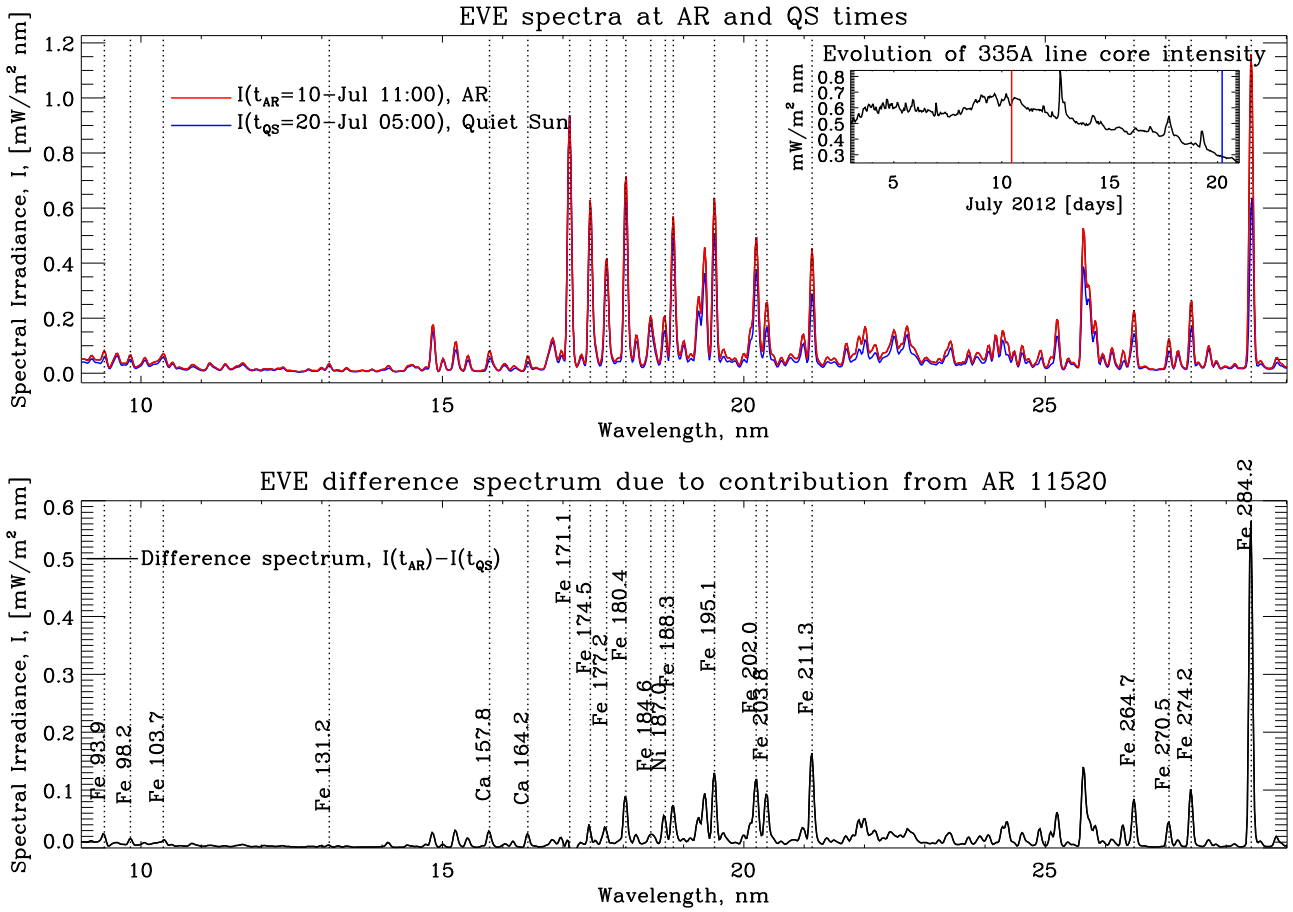

Figure 2. Top: EVE Sun-as-a-star spectra (spectral irradiances) at AR and quiet-Sun times, $I(\lambda, t_{AR})$ and $I(\lambda, t_{QS})$, repectively (red and blue colors); the top right panel shows evolution of the brightest Fe XVI 335 Å line core intensity, $I(\lambda = 335.45$ Å, $t)$, from July 3 to July 21. Bottom: EVE difference spectrum due to contribution from the AR alone at t_{AR}, $I(t_{AR}) - I(t_{QS})$. Dotted lines show spectral lines selected for the DEM analysis. See the line list in Table 1 and more details in Section 2.

17 day interval, with red and blue vertical lines marking t_{AR} and t_{QS}, respectively. For consistent comparison with irradiances, we did not account for magnetic field inclination nor foreshortening in $\Phi_{LOS}(t)$ calculation. We also ignored small contributions into $\Phi_{LOS}(t)$ and EVE irradiances from minor regions after t_{AR}, assuming that these originate from AR 11520. At the beginning of AR disk passage (before t_{AR}), other preceding regions dominate. The smooth variation of the LOS magnetic flux around the central meridian passage shows the dominance of this region and is consistent with the expected nearly vertical field orientation. Taking the difference of magnetic fluxes at the AR and quiet-Sun times, we evaluate the target region's LOS unsigned magnetic flux at t_{AR}, $\Phi_{LOS,AR}(t_{AR}) = \Phi_{LOS}(t_{AR}) - \Phi_{LOS}(t_{QS}) = 8 \times 10^{22}$ Mx. Alternatively, using a Mercator-deprojected HMI vector magnetic field map that includes the AR alone, we find a more accurate vertical (radial) unsigned magnetic flux $\Phi_{r,AR} = 11.8 \times 10^{22}$ Mx. Comparing this estimate with magnetic flux distributions from other known regions (see Figure 8 in Kazachenko et al. 2017), we characterize AR 11520 as a large region, with Φ_{AR} exceeding that of 80% of all solar ARs (for comparison the well-studied region AR 11158 had about 1/3 as much unsigned magnetic flux, 4×10^{22} Mx).

To track the region's evolution across the EUV spectrum, we used EVE spectral irradiances, $I(\lambda, t)$, from $t_{start} =$ 2012 July 3 09:00 UT to $t_{end} =$ 2012 July 20 00:00 UT. We chose an hourly cadence and derived 429 spectra in the range of 6.5–37 nm. When an AR passes across the solar disk, an enhancement is observed across the EUV spectrum. We used this enhancement to derive the *difference spectrum*, comparing t_{AR} to t_{QS} and thus isolating the target region alone; we can thus study its properties independent of the quiet-Sun background. This approach is not perfect because the presence of the region may itself alter the background spectrum; for this reason we have restricted our analysis to optically thin lines where this problem may not be significant.

Figure 2 shows the EVE spectrum (spectral irradiance) at t_{AR} and t_{QS}, namely $I(\lambda, t_{AR})$ and $I(\lambda, t_{QS})$ (top), and the difference spectrum due in principle to AR 11520 contribution alone at t_{AR}, $I(\lambda, t_{AR}) - I(\lambda, t_{QS})$ (bottom). The dotted lines correspond to 24 selected spectral lines, $\{\lambda_i\}$, that we chose to describe the EUV spectrum (see Table 1 for a line list).

To quantify the total flux in each line, taking into account possible line shifts and background offsets, we fitted the curve of each line with a Gaussian function. Figure 3 shows an example of Gaussian fits for 24 EVE spectral lines at t_{AR} and t_{QS}, respectively. We then integrated the spectral irradiance below each Gaussian around the line center to estimate the net irradiance corresponding to each spectral line at time t:

$$\Delta\Phi(\lambda_i, t) = \int_{\lambda_i} I(\lambda, t) d\lambda - \int_{\lambda_i} I(\lambda, t_{QS}) = \Phi(\lambda_i, t) - \Phi(\lambda_i, t_{QS}). \quad (1)$$

Figure 4 shows the result of this fitting: evolution of irradiances, $\Delta\Phi(\lambda_i, t)$, in 24 EVE lines corresponding to AR

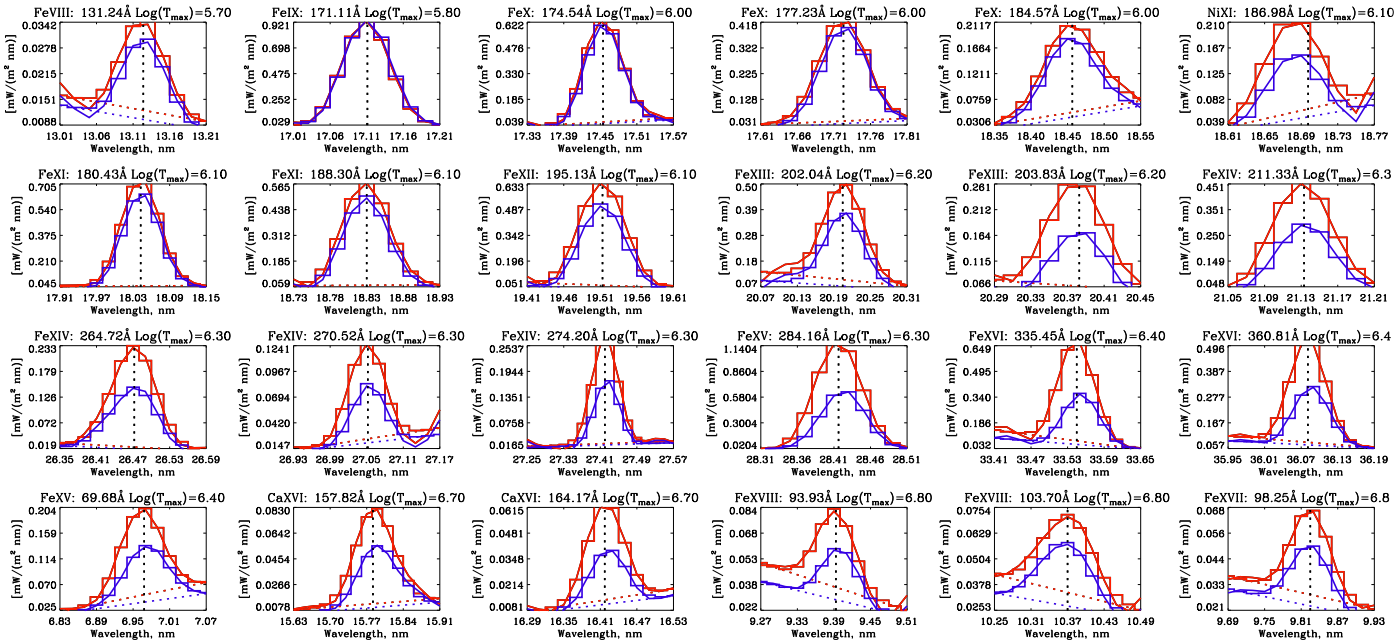

Figure 3. EVE line profiles (solid curves) with corresponding Gaussian fits at AR (t_{AR} = July 10 10:59 UT, red) and quiet-Sun (t_{QS} = July 20 04:59 UT, blue) times. Vertical and inclined dotted lines show the calculated line center location and the background value, respectively. See Section 2.

Table 1
The 24 EVE Lines and a Subset of Six AIA Target Lines (Marked with *) Initially Selected for the AR Analysis

i	Line (Å)	Ion	$\mathrm{Log}_{10}(T_{\max})$ (K)	$G_{\max}$, 10^{-24} (erg cm^{-3} s^{-1})
0	131.24*	Fe VIII	5.70*	2.00
1	171.11*	Fe IX	5.80*	49.47
2	174.54	Fe X	6.00	18.33
3	177.23	Fe X	6.00	10.28
4	184.57	Fe X	6.00	4.72
5	186.98	Ni XI	6.10	0.10
6	180.43	Fe XI	6.10	11.98
7	188.30	Fe XI	6.10	9.04
8	195.13*	Fe XII	6.10*	12.40
9	202.04	Fe XIII	6.20	3.79
10	203.83	Fe XIII	6.20	12.99
11	211.33*	Fe XIV	6.30*	6.03
12	264.72	Fe XIV	6.30	5.76
13	270.52	Fe XIV	6.30	2.28
14	274.20	Fe XIV	6.30	3.14
15	284.16	Fe XV	6.30	25.76
16	335.45*	Fe XVI	6.40*	12.03
17	360.81	Fe XVI	6.40	5.78
18	69.68	Fe XV	6.40	5.78
19	157.82	Ca XVI	6.70	0.02
20	164.17	Ca XVI	6.70	0.06
21	93.93*	Fe XVIII	6.80*	1.27
22	103.70	Fe XVIII	6.80	0.42
23	98.25	Fe XVIII	6.80	0.42

Note. Due to negative irradiance during AR evolution we further exclude the 171.11 Å line from our analysis, resulting in a final list of 23 EVE and five AIA lines. Columns correspond to each line wavelength, ion, temperature of the peak of the contribution function ($T_{\max}$), and the maximum value of the contribution function ($G_{\max}$). See Section 2.

11520 as it crossed the disk. Note how the 171.1 Å line irradiance dropped below zero as AR 11520 crossed the disk (panel 2, following the red line). These negative values are caused by "dark canopies" or "circumfacular regions" around the AR, which are darker that the quiet Sun in the 171.1 Å line. Originally discovered by Hale & Ellerman (1903) as a chromospheric effect, they also appear clearly in the nominally coronal 171 Å band (Wang et al. 2011), but without a detailed physical explanation yet. Since negative irradiances complicate the analysis, we exclude the 171.1 Å line from our further EVE data analysis, resulting in a final list of 23 EVE and five AIA lines (Hale & Ellerman 1903).

3. Methods: Finding the DEM and Radiated Energy using EVE Data

The flux differences we derive from EVE for each line, $\Delta\Phi(\lambda_i, t)$, are related to emissions as expressed in terms of the contribution function $G(\lambda_i, T_e, N_e)$, and the differential emission measure, $\mathrm{DEM}(T_e, t)$, by

$$\Delta\Phi(\lambda_i, t) = \frac{A_{\mathrm{AR}}}{4\pi R^2}\int_{T_e} G(\lambda_i, T_e, N_e)\mathrm{DEM}(T_e, t)dT_e, \quad (2)$$

where T_e and N_e are the electron temperature and number density and $G(\lambda_i, T_e, N_e)$ is computed with the CHIANTI v8 atomic database. To find $G(\lambda_i, T_e, N_e)$ we summed up contributions from each CHIANTI emission line within the ± 1 Å centered on the wavelength of each individual EVE line, assuming coronal abundances (Feldman 1992) and ionization equilibria (Mazzotta et al. 1998). Since EVE measures the irradiance in W m^{-2} nm^{-1} and $G(T)$ has units of erg cm^{-3} s^{-1}, to compare between the two we need to take into account the solid angle of the taken solar emission. Therefore in Equation (2) we divide the EVE irradiances, $\Phi(\lambda_i, t)$, by the approximate solid angle occupied by the area of the AR: $A_{\mathrm{AR}}/R^2 = 0.1A_{\mathrm{disk}}/R^2 = 0.1 \times 6.807 \times 10^{-5}$ sr, where A_{disk} is the solar disk area in cm^2, R is the Earth–Sun distance and 0.1 approximates the upper limit of the fraction of the solar disk occupied by the AR (see, e.g., Schonfeld et al. 2017). In Equation (2), $\mathrm{DEM}(T_e, t)$ (in units of cm^{-3} K^{-1}), describes the

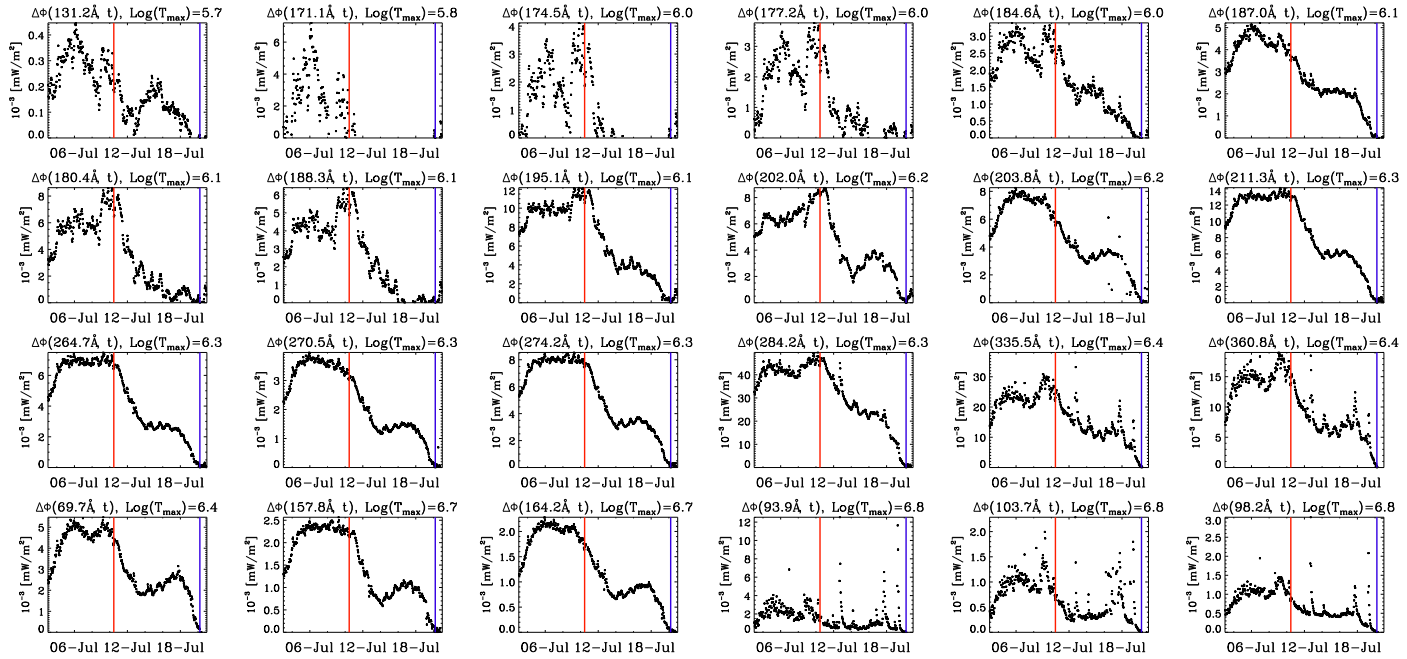

Figure 4. Evolution of AR 11520 irradiances (line-integrated EVE spectra), $\Delta\Phi(\lambda_i, t)$, from July 3 to July 21 for 24 EVE lines derived from a difference spectrum with respect to the quiet Sun (see Equation (1)). Vertical red and blue lines show t_{AR} and t_{QS}, respectively. See Section 2.

temperature distribution of plasma emitted along a distance along the LOS, s, at temperature T_e at time t,

$$\mathrm{DEM}(T_e, t) = N_e^2 ds/dT_e. \quad (3)$$

In this paper we use EVE irradiances, $\Delta\Phi(\lambda_i, t)$, to solve Equation (2) and derive $\mathrm{DEM}(T_e, t)$. Previously, many different DEM inversion methods have been developed and used to solve Equation (2) for DEM in flares and ARs using AIA/SDO (e.g., Hannah & Kontar 2012; Warren et al. 2012; Plowman et al. 2013; Cheung et al. 2015), EIS/Hinode (e.g., Testa et al. 2011; Tripathi et al. 2011; Warren et al. 2012; Petralia et al. 2014), Coronas-F (Reva et al. 2018), EVE/SDO (Schonfeld et al. 2017), and EVE/SDO and RHESSI (Caspi et al. 2014; McTiernan et al. 2019) data sets. In this paper we use the Hannah & Kontar (2012) inversion method with the EVE irradiances, $\Delta\Phi(\lambda_i, t)$, in either the full 23-line set or on a subset of five lines as identified in Table 1, and the $G(\lambda_i, T_e, N_e)$ functions from CHIANTI, to find the $\mathrm{DEM}(T_e, t)$ (Equation (2)). It is common to enforce positivity in the DEM solutions to prevent apparently nonphysical negative emission measures, but this may be mathematically incorrect for a difference spectrum in which negative values may occur naturally. For DEM inversions using the reduced set of five lines we find that the solutions obtained are uniformly positive even without this constraint, which is not the case when we use the full 23-line set in Table 1.

Finally, at each time t_i, we integrate over all coronal emission lines and $\mathrm{DEM}(T_e, t)$ to find the energy radiated by the AR plasma, the AR luminosity,

$$L_{AR}(t) = \int G_{tot}(T_e, N_e)\mathrm{DEM}(T_e, t)dT_e. \quad (4)$$

In this approach, to account for all coronal emission lines in the 1–300 Å range we sum CHIANTI contribution functions, $G_{tot}(T_e, N_e) = \sum_i G(\lambda_i, T_e, N_e)d\lambda$ using coronal abundances (Feldman 1992), ionization equilibria (Mazzotta et al. 1998), and a constant pressure (10^{15} cm^{-3} K) within a temperature range of $\mathrm{Log}_{10}T = [5.4, 7.5]$. Finally, integrating AR luminosity over time, we find the total AR radiative losses during 10 days of AR evolution from t_{AR} to t_{QS}.

$$E_{rad}(t) = \int_{t_{AR}}^{t_{QS}} L_{AR}(t)dt. \quad (5)$$

4. Results

4.1. Active Region DEM: EVE versus AIA Observations

To test our approach of using EVE measurements to find the DEM, we first calculate a DEM from the EVE difference spectrum and compare it with one derived from the full-disk AIA images (Figure 5). To make a direct comparison we first derive the DEM from EVE data using the reduced set of five spectral lines: 131.2, 195.1, 211.3, 335.5, and 93.9 Å. We exclude the 171.1 Å line from our analysis since its difference irradiance, $\Delta\Phi(\lambda_i, t_{AR})$, dropped below zero as AR 11520 crossed the disk (see Figure 4, panel 2 for 171.1 Å). For AIA intensities we use full-disk averaged intensity differences, $\bar{I}_{AIA,\lambda}(t_{AR}) - \bar{I}_{AIA,\lambda}(t_{QS})$. For AIA emissivities we use the AIA response function (Boerner et al. 2012). To find the DEM we choose a range of temperatures, $\mathrm{Log}_{10}T = [5.4, 7.5]$, binned into 53 segments.

Figure 5 shows an example of two DEMs, $\mathrm{DEM}(T_e, t_{AR})$, derived from difference fluxes from EVE (five lines) and AIA (six bands), $\Delta\Phi(\lambda_i, t_{AR})$ (see Equation (1)), respectively. The middle panel shows EVE contribution functions corresponding to each line. Notice that even though many lines can be considered isothermal, they have significant emission over a range of temperatures due to contributions from other lines within ±1 Å centered on each individual EVE line (see the $G(\lambda, T_e, N_e)$ description in Section 3). The right panel shows the comparison between observed and DEM-reconstructed EVE fluxes, as a validation test for the DEM inversion. From

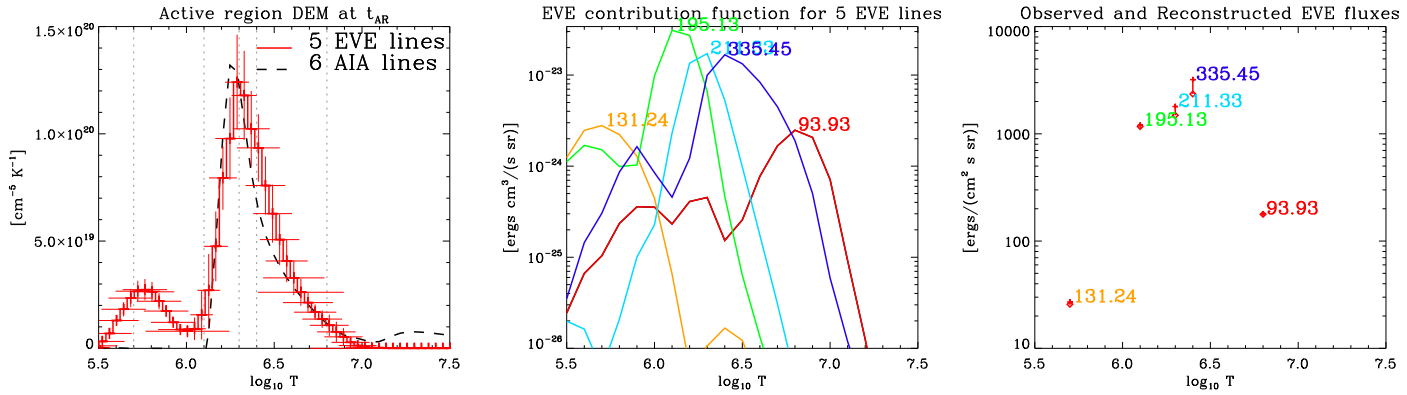

Figure 5. Left: calculated AR DEM using five EVE lines (red) and six AIA bands (dashed black) at t_{AR} = July 10 10:59 UT. Middle: CHIANTI contribution functions, $G(\lambda_i, T_e, N_e)$, for five selected EVE lines. To find them we summed up contribution functions from each CHIANTI emission line within ±1 Å from the line center (see Section 3). Right: EVE irradiances, $\Delta\Phi(\lambda_i, t_{AR})$, observed and reconstructed from the DEM. See Section 4.1.

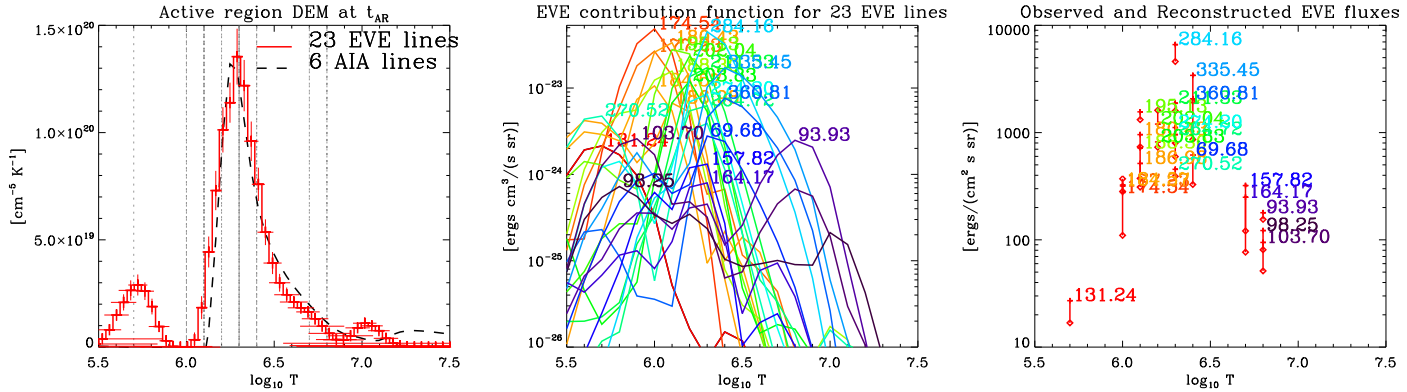

Figure 6. Left: calculated AR DEM using the 23 EVE lines (red) and six AIA bands (dashed black) at t_{AR} = July 10 10:59 UT. Middle: CHIANTI contribution functions for the 23 lines. Right: EVE irradiances, $\Delta\Phi(\lambda_i, t_{AR})$, observed and reconstructed from the DEM. See Section 4.1.

this comparison, we conclude that the EVE and AIA data sets result in similar DEM estimates, validating our working hypothesis of using EVE Sun-as-a-star measurements to derive thermal properties of an evolving AR in the absence of other solar activity on the disk. The coarse wavelength set for EVE resulted in a minor discrepancy at the lowest temperatures.

In Figure 6 we also calculate the AR's DEM when it is at the disk center using all 23 EVE lines instead of the five-line subset as above. We compare DEMs from 23 EVE lines with DEM derived using six bands from AIA and also find that the two agree well, but note that the errors for the 23-line inversion are larger (compare, e.g., the 131 and 94 Å lines' validation on the right panels of Figures 5 and 6). These larger errors might lead to nonrealistic DEM inversions (see, e.g., a small DEM increase around $\mathrm{Log}_{10}T = 7$ in the 23-line inversion). Moreover, the selection of suitable lines for DEM analysis is critical since the detailed atomic characteristics associated with the chosen emission lines must be fully characterized to properly calculate the DEM. Since CHIANTI lacks a large number of weak unresolved lines that appear in the EVE spectrum, we further restrict our analysis of DEM evolution to only five emission lines, shown in Figure 5, that are best characterized.

4.2. Active Region Irradiance Evolution

Figure 7 (left panel) shows the evolution of the derived AR DEM(T_e, t) from 2012 July 10 to July 20. The panels on the right show the quality of the DEM reconstruction: a comparison between EVE input difference fluxes and the fluxes reconstructed from the DEM. The validation time series match each other closely, including the hot enhancements during flares, with the Spearman correlation coefficient ranging from 0.96 to 1.0 for the five selected lines. We find the worst differences (up to 20% for 211 Å and 30% for 335 Å lines), corresponding to $\mathrm{Log}_{10}(T_{max}) = [6.3, 6.4]$. These discrepancies serve as uncertainty estimates, complementing contributions from the calibration of the EVE irradiance spectra (5%–7% for the strongest lines, Hock et al. 2012), error estimation of line fluxes from our Gaussian fits to the EVE spectra (several percent depending on the line), any density sensitivity in the DEM estimates, plus the acknowledged uncertainties in the CHIANTI atomic data. We estimate an overall uncertainty in the DEMs to be less than 40%, exclusive of the possibly comparable uncertainties in the atomic data (Dere et al. 1997).

In Figure 8 we show how the EUV irradiance and luminosity evolve during the 10 days of AR evolution, $I_{AR}(t)$ and $L_{AR}(t)$. To estimate L_{AR}(t) (top right panel), we use Equation (4), using the EVE-derived DEM(T_e, t) (see Figure 7) and the total contribution function, $G_{tot}(T_e, N_e) = \sum_i G(\lambda_i, T_e, N_e)d\lambda$, using CHIANTI data in the 1–300 Å range (top left panel). We find the mean AR 11520 irradiance to be $\bar{I}_{AR} = 2.3 \times 10^5$ erg (cm^{-2} s^{-1}), and the luminosity to be $\bar{L}_{AR} = 3.5 \times 10^{26}$ erg s^{-1} $= 10^{26.5}$ erg s^{-1} (see horizontal dotted lines on the top right and bottom left panels, respectively). Integrating L_{AR} over

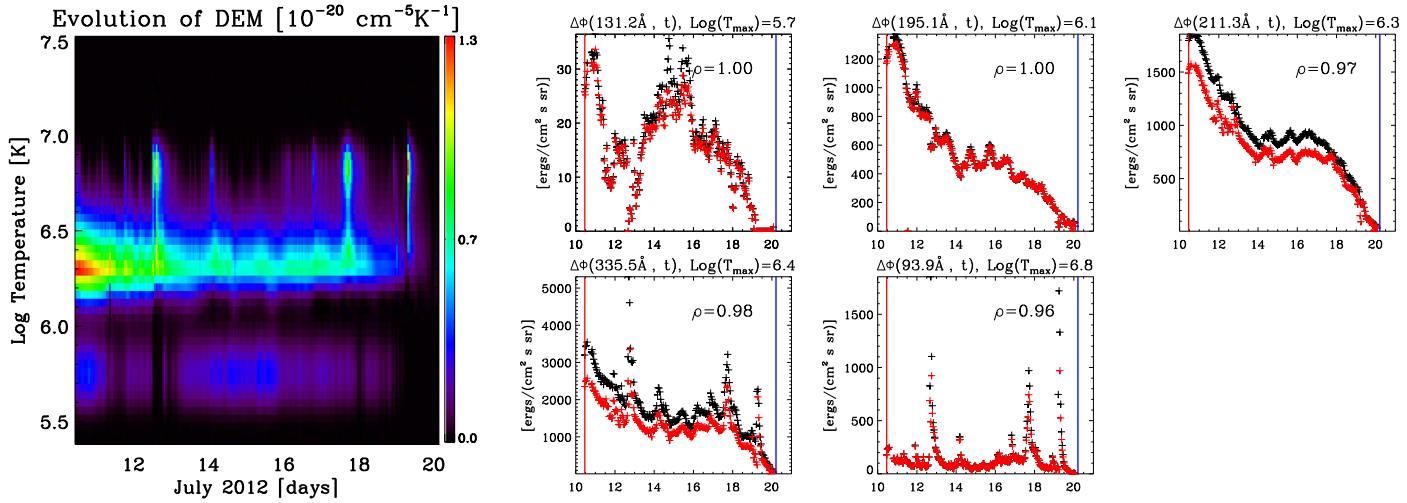

Figure 7. Left: the evolution of the AR 11520 DEM(t, T_e), represented as a a spectrogram. Note the occasional extensions to higher temperatures associated with flares, such as on 2012 July 12 when an X1.4 flare occurred. Right: quality of the DEM reconstruction. Observed EVE input fluxes (black) and fluxes reconstructed from the DEM (red) vs. time; ρ in the top right corner shows a Spearman correlation coefficient between the EVE input and DEM-reconstructed output fluxes. See Section 4.2.

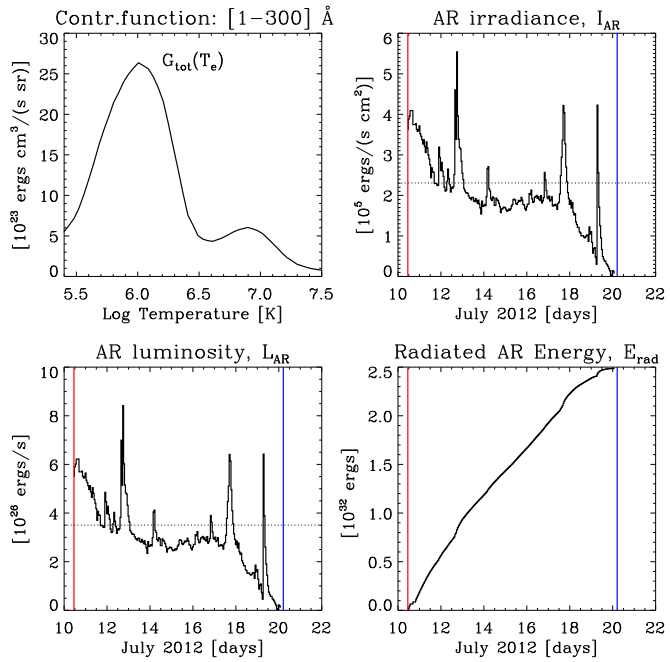

Figure 8. Top row: total CHIANTI contribution function, $G_{\rm tot}(T_e, N_e) = \sum_i G(\lambda_i, T_e, N_e) d\lambda$, in the 1–300 Å range and derived AR 11520 irradiance, $I_{\rm AR}$. Bottom row: AR luminosity, $L_{\rm AR}$, and cumulative AR radiative losses, $E_{\rm rad}$. Horizontal dotted lines show the mean values of $\bar{I}_{\rm AR} = 6 \times 10^6$ erg s^{-1} and $\bar{L}_{\rm AR} = 9 \times 10^{27}$ erg s^{-1}, when AR 11520 was present on the solar disk (from July 10 to July 18). See Section 4.2.

10 days, we find the total radiative energy losses of AR 11520 during the 10 days of AR evolution to be $E_{\rm rad} = 2.5 \times 10^{32}$ erg in the 1–300 Å range.

For comparison, the range of solar cycle variation of the luminosity of the Sun in this spectral range has been estimated at 3×10^{25} erg s^{-1} to 10^{27} erg s^{-1} (Haisch & Schmitt 1996; Huensch et al. 1998; Hünsch et al. 1999). Acton (1996) used Yohkoh/Soft X-ray Telescope (SXT) data converted to the "RASS" [0.1–2.4] keV ([5.2–123] Å) ROSAT/PSPC passband to find similar estimates; these were later adjusted by Haisch & Schmitt (1996) to increase the minimum value to 10^{26} erg s^{-1}. Ayres (1997) used suborbital rocket measurements in a narrower passband, [6–62] Å (0.2–2 keV), to obtain higher variations from 5×10^{26} to 2×10^{27} erg s^{-1}. Finally, Judge et al. (2003) also used measurements from the Solar X-Ray Photometer (SXP) instrument on board the Student Nitric Oxide Explorer (SNOE) in the RASS passband to estimate variations from 6.3×10^{26} to 7.9×10^{27} erg s^{-1}. To relate our estimates of AR luminosity with stellar and solar cycle variations, we also evaluate radiative loss rates over the RASS passband. We find the mean AR 11520 luminosity, $\bar{L}_{\rm AR,(3-124)} = 1.4 \times 10^{26}$ erg s^{-1}, which is some five times smaller than the minimum range of the solar cycle variation, 6.3×10^{26} erg s^{-1}, reported by Judge et al. (2003), and therefore roughly in concordance given the common occurrence of multiple active regions during solar maximum.

In addition, we compare our region's luminosity to the magnetic energy flux through the photosphere, the Poynting flux S_z, 1 hr before $t_{\rm AR}$. Figure 9 shows the spatial distribution of S_z in AR 11520. To calculate $S_z = -\boldsymbol{E_h} \times \boldsymbol{B_h}$ we use the horizontal component of the electric field vector, $\boldsymbol{E_h}$, from the inversion method PTD-Doppler-FLCT-Ideal inversion method (PDFI, where PTD stands for poloidal-toroidal decomposition and FLCT for Fourier Local Correlation Tracking, Kazachenko et al. 2014, 2015), and the horizontal component of the vector magnetic field $\boldsymbol{B_h}$, on July 10 09:48 UT. We find that the majority of the AR magnetic energy at the photosphere is injected at positive and negative vertical Poynting fluxes, $S_z \approx [10^7, 10^8]$ erg cm^{-2} s^{-1}, with a total AR-integrated energy injection rate, $E_{\rm mag}(t_{\rm AR}) = \int_{\rm AR} S_z dS = 3 \times 10^{28}$ erg s^{-1}. Note that here we only estimate the energy injection rate $E_{\rm mag}$ at one time, when the AR was close to the disk center. However, as we have seen from a study of magnetic energy fluxes in AR 11158, $E_{\rm mag}(t)$ varies significantly as a function of time. For AR 11158 we found a mean $\bar{E}_{\rm mag} = 5 \times 10^{27}$ erg s^{-1} during 5 days of this region's evolution, varying from -6 to 18×10^{27} erg s^{-1} (see Figure 9 in Kazachenko et al. 2015). If we

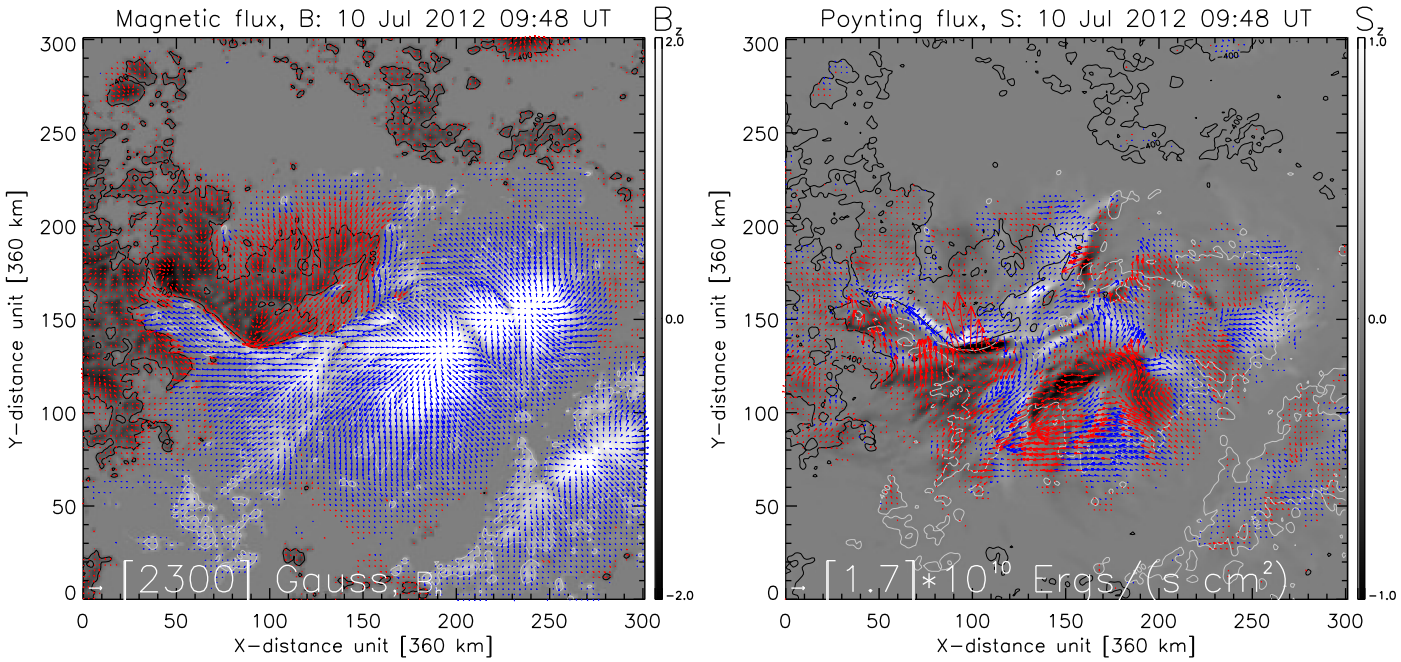

Figure 9. AR 11520 vector magnetic field (left) and the PDFI energy flux vector through the photosphere (right) on July 10 2012, 09:48 UT. The B_z and S_z gray-scale color scales vary from −2000 to 2000 G and -10^{10} to 10^{10} erg cm^{-2} s^{-1}, respectively. See Section 4.2.

assume that our instantaneous estimates of $E_{\rm mag}(t_{\rm AR})$ and $S_z(t_{\rm AR})$ approximate the mean magnetic energy injection rate at the photosphere, as AR 11520 evolved, then we conclude that both typical Poynting fluxes, $S_z(t_{\rm AR}) \approx [10^7, 10^8]$ erg cm^{-2} s^{-1}, and the mean magnetic energy injection rate, $E_{\rm mag}(t_{\rm AR}) = 3 \times 10^{28}$ erg s^{-1}, are around two orders of magnitude larger than the mean AR irradiance, $\bar{I}_{\rm AR} = 2.3 \times 10^5$ erg cm^{-2} s^{-1}, and the AR luminosity, $\bar{L}_{\rm AR} = 3.5 \times 10^{26}$ erg s^{-1}, derived above.

Finally, we compare our mean AR luminosity to AR unsigned magnetic flux, $\bar{L}_{\rm AR}$ and $\Phi_{\rm LOS,AR}$. Previously, Fisher et al. (1998) used a Mees Solar Observatory (MSO) vector magnetic field and Yohkoh SXT X-ray observations in 333 ARs between 1991–1995 to find a relationship between magnetic fields and coronal heating. They deduced a scaling law between AR luminosities (in 1–300 Å) and unsigned magnetic fluxes, $L_{\rm AR} \approx 1.2 \times 10^{26}$ erg s^{-1} $(\Phi_{\rm AR}/10^{22}$ Mx$)^{1.19}$. Note that Fisher et al. (1998) used a simplified single-temperature approach ($\mathrm{Log}_{10}T = 6.5$ or $T = 3 \times 10^6$ K) resulting in errors in $L_{\rm AR}$ up to a factor of 2. Here, in contrast, we use a more accurate multitemperature DEM approach to estimate the AR luminosity. We compare our estimates of mean AR luminosity and magnetic flux as AR crossed the disk, $\bar{L}_{\rm AR} = 3.5 \times 10^{26}$ erg s^{-1} and $\Phi_{\rm LOS,AR} = 8 \times 10^{22}$ Mx. We find that our $\bar{L}_{\rm AR}$ is four times smaller than the one expected for a given $\Phi_{\rm LOS,AR}$ from the scaling law above, but is in agreement with the overall scatter of $(L_{\rm AR} - \Phi_{\rm AR})$ shown in Figure 9 of Fisher et al. (1998). Note that here we only compared mean values of $(L_{\rm AR} - \Phi_{\rm AR})$, instead of their evolution, since neither of these variables exhibited much variability apart from variations due to solar rotation. We would also like to note that our AR magnetic flux is above the range of AR magnetic fluxes in Fisher et al. (1998). Comparing unsigned magnetic fluxes in Fisher et al. (1998) from MSO and in Kazachenko et al. (2017) from SDO, we find that the SDO values are around five times larger than the MSO values, a discrepancy that might be interesting to explore in future.

5. Conclusions

We have evaluated the radiative losses during a quiescent period of the evolution of AR 11520. For this we used hourly Sun-as-a-star spectra from EVE/SDO in the 6.5–37 nm range during 10 days, as this fairly large AR 11520 ($\Phi_{\rm LOS,AR} = 8 \times 10^{22}$ Mx) was crossing the solar disk. Since AR 11520 was the only major region on the solar disk, we could use EVE difference fluxes, $\Delta\Phi(\lambda_i, t) = \Phi(\lambda_i, t) - \Phi(\lambda_i, t_{\rm QS})$, to derive its DEM. Specifically, we used a set of five iron emission lines that sample the AR coronal temperature range from 0.5–6.3 MK ($\mathrm{Log}_{10}T = [5.7, 6.8]$) and have well-studied atomic properties and minimal blending. We then applied this approach to a sequence of EVE spectra to derive a sequence of DEMs during 10 days of AR evolution (see Figure 7). From the derived evolution of DEM we determined the AR radiative losses as a function of time (see Figure 8). Our findings are as follows.

1. We find that the shape and the peak temperature of the DEM, as extracted from EVE data, are overall consistent with previous studies using spatially resolved observations of quiescent regions (e.g., Tripathi et al. 2011; Warren et al. 2012; Petralia et al. 2014). Our DEM peaks at $\mathrm{Log}_{10}T = 6.3$, corresponding to a relatively cool AR plasma. The peak temperature stays nearly constant as the AR evolves, illustrating the slowly varying nature of irradiance of the region studied. The DEM does exhibit high-temperature enhancements during flares. However, since our 1 hr cadence of EVE data is too sparse for describing flare contributions, we have ignored them in this analysis.
2. We find that the mean AR irradiance during 10 days of AR evolution in the 1–300 Å spectral range is $\bar{I}_{\rm AR} = 2.3 \times 10^5$ erg cm^{-2} s^{-1}. This estimate is around 20 times smaller than the classical Withbroe & Noyes (1977) estimate of the bolometric radiative flux in such a region, $I_{\rm AR,W\&N} = 5 \times 10^6$ erg cm^{-2} s^{-1}. Note, however, that

our estimate does not include the optically thick component (essentially, the chromosphere), which Withbroe & Noyes (1977) estimate at about twice the magnitude of the optically thin coronal component. The remainder of the discrepancy presumably relates to the scaling of AR area.

3. Integrating over the whole AR, we find a mean AR radiative energy loss rate during 10 days of AR evolution, $\bar{L}_{\rm AR} = 3.5 \times 10^{26}$ erg s^{-1}. We compare it with the magnetic energy flux through the photosphere, when the AR is close to the disk center, $S_{\rm z,mag} = [10^7, 10^8]$ erg cm^{-2} s^{-1}, or integrating over the whole AR, a total energy flux of $E_{\rm mag} = 3 \times 10^{28}$ erg s^{-1}. We conclude that the coronal radiative energy losses within 1–300 Å comprise about 1% of the available magnetic energy flux, confirming the relative importance of the chromospheric heating problem.
4. To relate our estimates of AR luminosity with stellar and solar cycle variations, we evaluate radiative loss rates over the 3–124 Å ROSAT-PSPC passband. We find a mean AR 11520 luminosity, $\bar{L}_{\rm AR,(3-124)} = 1.4 \times 10^{26}$ erg s^{-1}, which is five times smaller than the minimum range of the solar cycle variation, 6.3×10^{26} erg s^{-1}, reported by Judge et al. (2003).
5. We find AR 11520 total cumulative radiated energy, $E_{\rm rad} = 2.5 \times 10^{32}$ erg, during 10 days of evolution. This estimate is an order of magnitude larger or similar to bolometric radiated energies associated with M- and X-class flares (Emslie et al. 2012, $E_{\rm bol} \approx 10^{30}$–$10^{31}$ erg), highlighting the importance of AR radiative losses in AR and flare energetics.
6. Finally, we compare our mean AR luminosity to AR unsigned magnetic flux. We find these to be consistent with a previously derived statistical relationship, $L_{\rm AR} \sim \Phi_{\rm AR}^{1.19}$, using a more simplified single-temperature approach (Fisher et al. 1998). We therefore confirm that this relationship could be further used in both solar and stellar astronomy, when only one kind of observation is available.
7. This study is the first detailed analysis of AR thermal properties using EVE/SDO Sun-as-a-star observations. Our novel approach opens doors to similar studies of active regions on other stars where spatial resolution is an issue (e.g., France et al. 2019).

To conclude, our analysis demonstrates that AR coronal radiative losses are ∼100 times smaller than the typical magnetic energy fluxes at the photosphere, but nevertheless are significant compared to flare radiative losses. Although this study did not include chromospheric losses, Withbroe & Noyes (1977) estimate these at about twice the coronal contribution, and the majority of the magnetic energy supply may therefore wind up in faculae. Future synergetic studies of energy cycle in active regions, including magnetic energy fluxes through the photosphere and coronal energy losses during both quiescent and active periods of AR evolution (e.g., Iglesias et al. 2019), will enable our understanding of AR energetics that may be overlooked in isolated studies of flaring or quiescent periods of ARs.

We thank Richard C. Canfield for illuminating discussions that have triggered this project. We thank the EVE and AIA teams for providing us with the SDO/EVE and SDO/AIA data sets. We thank the US taxpayers for providing the funding that made this research possible. We acknowledge support from NASA LWS NNH17ZDA001N and 80NSSC19K0070 (M.D. K), NASA 80NSSC18K1283-HSR (M.D.K) and NASA ECIP NNH18ZDA001N (M.D.K.). H.S.H. thanks the University of Glasgow for hospitality.

ORCID iDs

Maria D. Kazachenko https://orcid.org/0000-0001-8975-7605
Hugh S. Hudson https://orcid.org/0000-0001-5685-1283

References

Acton, L. 1996, in ASP Conf. Ser., 109, Comparison of YOHKOH X-ray and other solar activity parameters for November 1991 to November 1995, ed. R. Pallavicini & A. K. Dupree (San Francisco, CA: ASP), 45
Ayres, T. R. 1997, JGR, 102, 1641
Boerner, P., Edwards, C., Lemen, J., et al. 2012, SoPh, 275, 41
Caspi, A., McTiernan, J. M., & Warren, H. P. 2014, ApJL, 788, L31
Cheung, M. C. M., Boerner, P., Schrijver, C. J., et al. 2015, ApJ, 807, 143
Démoulin, P., Mandrini, C. H., van Driel-Gesztelyi, L., et al. 2002, A&A, 382, 650
Dere, K. P., Landi, E., Mason, H. E., Monsignori Fossi, B. C., & Young, P. R. 1997, A&AS, 125, 149
Emslie, A. G., Dennis, B. R., Shih, A. Y., et al. 2012, ApJ, 759, 71
Feldman, U. 1992, PhyS, 46, 202
Fisher, G. H., Longcope, D. W., Metcalf, T. R., & Pevtsov, A. A. 1998, ApJ, 508, 885
France, K., Fleming, B. T., Drake, J. J., et al. 2019, Proc. SPIE, 11118, 1111808
Haisch, B., & Schmitt, J. H. M. M. 1996, PASP, 108, 113
Hale, G. E., & Ellerman, F. 1903, PYerO, 3, I.1
Hannah, I. G., & Kontar, E. P. 2012, A&A, 539, A146
Hock, R. A., Woods, T. N., Klimchuk, J. A., Eparvier, F. G., & Jones, A. R. 2012, arXiv:1202.4819
Huensch, M., Schmitt, J. H. M. M., & Voges, W. 1998, A&AS, 132, 155
Hünsch, M., Schmitt, J. H. M. M., Sterzik, M. F., & Voges, W. 1999, A&AS, 135, 319
Iglesias, F. A., Cremades, H., Merenda, L. A., et al. 2019, AdSpR, 65, 1641
Judge, P. G., Solomon, S. C., & Ayres, T. R. 2003, ApJ, 593, 534
Kazachenko, M. D., Fisher, G. H., & Welsch, B. T. 2014, ApJ, 795, 17
Kazachenko, M. D., Fisher, G. H., Welsch, B. T., Liu, Y., & Sun, X. 2015, ApJ, 811, 16
Kazachenko, M. D., Lynch, B. J., Welsch, B. T., & Sun, X. 2017, ApJ, 845, 49
Lemen, J. R., Title, A. M., Akin, D. J., et al. 2012, SoPh, 275, 17
Liu, Y., & Schuck, P. W. 2012, ApJ, 761, 105
Lumme, E., Kazachenko, M. D., Fisher, G. H., et al. 2019, SoPh, 294, 84
Mazzotta, P., Mazzitelli, G., Colafrancesco, S., & Vittorio, N. 1998, A&AS, 133, 403
McTiernan, J. M., Caspi, A., & Warren, H. P. 2019, ApJ, 881, 161
Ortiz, A., Domingo, V., Sanahuja, B., & Fröhlich, C. 2004, JASTP, 66, 67
Pesnell, W. D., Thompson, B. J., & Chamberlin, P. C. 2012, SoPh, 275, 3
Petralia, A., Reale, F., Testa, P., & Del Zanna, G. 2014, A&A, 564, A3
Plowman, J., Kankelborg, C., & Martens, P. 2013, ApJ, 771, 2
Reva, A., Ulyanov, A., Kirichenko, A., Bogachev, S., & Kuzin, S. 2018, SoPh, 293, 140
Schonfeld, S. J., White, S. M., Hock-Mysliwiec, R. A., & McAteer, R. T. J. 2017, ApJ, 844, 163
Schou, J., Scherrer, P. H., Bush, R. I., et al. 2012, SoPh, 275, 229
Testa, P., Reale, F., Landi, E., DeLuca, E. E., & Kashyap, V. 2011, ApJ, 728, 30
Tripathi, D., Klimchuk, J. A., & Mason, H. E. 2011, ApJ, 740, 111
Tziotziou, K., Georgoulis, M. K., & Liu, Y. 2013, ApJ, 772, 115
Ugarte-Urra, I., Warren, H. P., Upton, L. A., & Young, P. R. 2017, ApJ, 846, 165
van Driel-Gesztelyi, L., & Green, L. M. 2015, LRSP, 12, 1
Vemareddy, P. 2015, ApJ, 806, 245
Wang, Y. M., Robbrecht, E., & Muglach, K. 2011, ApJ, 733, 20
Warren, H. P., Winebarger, A. R., & Brooks, D. H. 2012, ApJ, 759, 141
Withbroe, G. L., & Noyes, R. W. 1977, ARA&A, 15, 363
Woods, T. N., Eparvier, F. G., Hock, R., et al. 2012, SoPh, 275, 115
Zahid, H. J., Hudson, H. S., & Fröhlich, C. 2004, SoPh, 222, 1